Primary hematite in Neoarchean to Paleoproterozoic oceans

Si Sun[1], Kurt O. Konhauser[2], Andreas Kappler[3], and Yi-Liang Li[1,†]

[1]*Department of Earth Sciences, University of Hong Kong, Hong Kong, China*

[2]*Department of Atmospheric and Earth Sciences, University of Alberta, Edmonton, Alberta T6G 2E3, Canada*

[3]*Geomicrobiology Group, Center for Applied Geosciences, University of Tübingen, Sigwartstrasse 10 72076, Tübingen, Germany*

ABSTRACT

Banded iron formations (BIFs) are iron- and silica-rich chemical sedimentary rocks formed throughout the Archean and Paleoproterozoic Eras. The presence of hematite (Fe_2O_3) and magnetite (Fe_3O_4) in BIFs has led to the widespread assumption that Fe(II) oxidation must have occurred in the ancient oceans via either a biological or chemical mechanism. However, it is unclear whether the ferric iron now present in BIF represents the original ferric oxyhydroxide [e.g., ferrihydrite, $Fe(OH)_3$] precipitated in the water column, or if it is the result of later-stage circulation of oxidizing fluids through the sediment pile. In this study, we conducted high-resolution microscopic investigations on BIF from the 2728 Ma Abitibi greenstone belt located in the Superior Province of the Canadian Shield and the 2460 Ma Kuruman Iron Formation in South Africa to ascertain the timing and paragenesis of the hematite. Three types of hematite are identified by high-resolution electron microscopic characterization and selected area electron diffraction: (1) 3–5 nm ultrafine hematite particles in the iron oxide–rich bands (H1); (2) submicrometer subhedral to euhedral hematite crystals randomly distributed in the chert matrix of transitional zones between iron oxide– and chert-rich bands (H2); and (3) needle-like, radial and fibrous hematite that replaced stilpnomelane or carbonates and is distributed along fractures or layer boundaries (H3). We interpret the first two types as primary minerals dehydrated from precursor ferric oxyhydroxides. H1 remains ultrafine in size, while H2 has undergone an Ostwald coarsening process facilitated by internal fluids produced during amorphous silica to quartz transformation. H3 is a later-stage mineral formed by external fluid-mediated replacement of iron silicates or carbonates. These results indicate that a significant fraction of the hematite in the BIF originated from ferric oxyhydroxide precursors. Importantly, this implies that photosynthetic Fe(II) oxidation, by either a direct or indirect biological mechanism, did exist in seawaters from which some BIF material was deposited.

†yiliang@hku.hk.

INTRODUCTION

Banded iron formations (BIFs) are chemical sedimentary rocks characterized by alternating silica- and iron-rich bands (e.g., Beukes and Klein, 1990; Klein, 2005; Bekker et al., 2010; Li, 2014). The least metamorphosed BIFs commonly consist of chert, magnetite, hematite, carbonates (siderite, dolomite-ankerite), greenalite, stilpnomelane, and riebeckite (Bekker et al., 2014). None of these minerals represents original BIF sediment; rather, they formed during diagenesis and metamorphism (e.g., Bekker et al., 2010, 2014). For instance, chert (microcrystalline quartz) was initially deposited as amorphous silica, or as silica flocculated with ferric oxyhydroxides (e.g., Siever, 1957, 1992; Fischer and Knoll, 2009). In terms of the iron component, the presence of both ferric and ferrous iron-containing minerals gives BIFs an average oxidation state of $Fe^{2.4+}$ (Klein and Beukes, 1992). Whether this redox state represents that of the water column from which the primary materials precipitated, or whether it represents postdepositional alteration remains unclear. The uncertainty largely stems from the controversial origin of hematite, or for that matter, ferric iron in BIFs. It is generally accepted that hematite in the unmineralized BIF sediments is a dehydration product of a ferrihydrite precursor (Ahn and Buseck, 1990; Morris, 1993; Pecoits et al., 2009; Bekker et al., 2010) precipitated in the photic zone via enzymatic Fe(II) oxidation (e.g., Widdel et al., 1993; Konhauser et al., 2002; Kappler et al., 2005) or O_2-oxidation facilitated by cyanobacteria (e.g., Konhauser et al., 2002, 2007). However, it has also recently been suggested that the primary precipitates of BIFs were microgranules (<~4 µm) of iron silicates similar to smectite rather than ferric oxyhydroxides, and hematite was a result of postlithification fluid circulation during which the infiltrated O_2-bearing meteoric fluids oxidized ferrous iron to hematite (Krapež et al., 2003; Rasmussen et al., 2013, 2014). In this scenario, the ocean should have been more reducing than previously suggested (Rasmussen et al., 2014).

To provide new insights into this issue, we report here on petrographic observations and detailed high-resolution electron microscopic investigations of hematite from two major minimally metamorphosed BIFs: the (1) uppermost part of the Hunter Mine Group in the Abitibi greenstone belt in Canada, and (2) Kuruman Iron Formation of the Transvaal Supergroup in South Africa.

GEOLOGICAL BACKGROUND AND SAMPLES

The Abitibi belt is the world's largest Archean greenstone belt (300 × 700 km^2) located in the Superior Province of the Canadian Shield (Fig. 1). It is an arc terrain composed of volcanic successions (Mueller et al., 1996, 2009). Based on lithology and tectonic and metamorphic evolutionary histories, the Abitibi greenstone belt was divided into northern and southern volcanic zones (Chown et al., 1992). The Hunter Mine Group is located on the southern margin of the northern volcanic zone, which, is bounded by the east-trending Destor-Porcupine-Manneville fault (Fig. 1). Overlain by the Stoughton-Roquemaure Group, the Hunter Mine Group is a complex of volcanic and sedimentary rocks, locally displaced by north-trending faults or intruded by dikes (Fig. 1, e.g., Mueller et al., 1996; Mueller and Mortensen, 2002). U-Pb and $^{207}Pb/^{206}Pb$ zircon chronology of the volcanic rocks and dikes indicates that the Hunter Mine Group has undergone three volcanic evolutionary stages: 2734–2730 Ma lower forma-

GSA Bulletin; May/June 2015; v. 127; no. 5/6; p. 850–861; doi: 10.1130/B31122.1; 9 figures; 1 table; published online 22 January 2015.

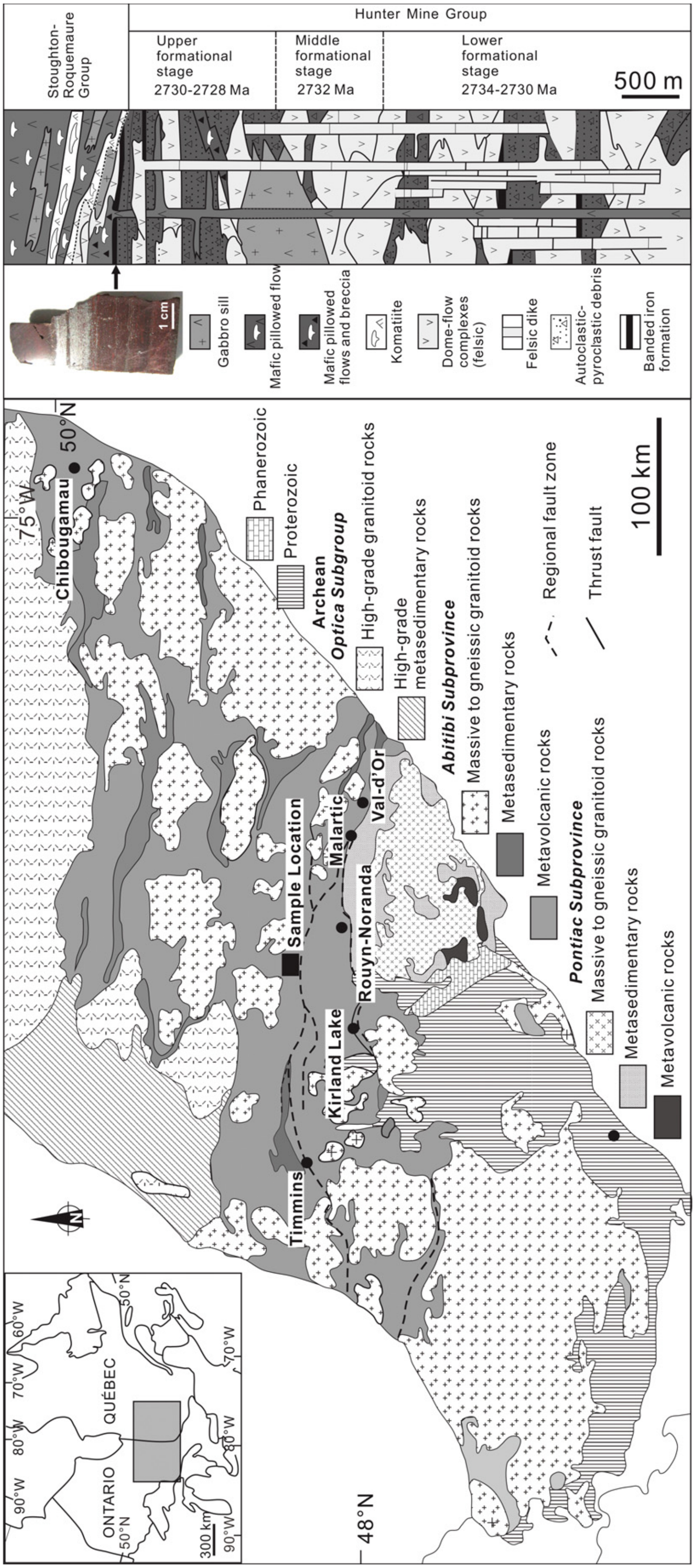

Figure 1. Geological setting of the Abitibi greenstone belt and stratigraphic column showing the placement of the Hunter Mine Group (after Powell et al., 1995; Mueller and Mortensen, 2002).

tional stage, 2732 Ma middle formational stage, and 2730–2728 Ma upper formational stage (Fig. 1; Mueller and Mortensen, 2002). Oxide (chert-jasper-magnetite) and carbonate facies BIFs constitute part of the Hunter Mine Group. Previous field studies have shown that the two BIF facies are only spatially but not temporally related (e.g., Chown et al., 2000). The oxide facies was directly derived from fluids seeping from volcanic sediments during periods of volcanic quiescence, whereas the carbonate facies formed by in situ hydrothermal replacement of chert-tuff beds (e.g., Chown et al., 2000). It was further suggested that only the oxide facies could be used as an indicator of the depositional environment, and its age could be approximated from the hosting volcanic rocks as 2730–2728 Ma (Chown et al., 2000; Mueller and Mortensen, 2002). The Abitibi BIF used in this study is from the oxide facies iron formation in the uppermost part of the Hunter Mine Group (Fig. 1). The whole Abitibi belt was metamorphosed to subgreenschist to greenschist facies during a regional metamorphism event that postdated movements along the Porcupine-Destor fault (Powell et al., 1995).

The Transvaal Supergroup in South Africa consists of the Ghaap and Postmasburg Groups. The Ghaap Group is overlain by a diamictite (interpreted as glacial till) with low-angle unconformity, and it is underlain by the ca. 2715 Ma Ventersdorp Supergroup. It is subdivided into Campbellrand and Asbestos Hill Subgroups (Beukes, 1984). The Kuruman Iron Formation is from the Asbestos Hill Subgroup, consisting of ankerite and banded chert at its base, with rhythmically banded chert, iron oxides, and siderite at its middle part, and intraclastic BIF at its top. The Kuruman BIF sampled for this study is a drill core collected from the middle part of the Kuruman Iron Formation near the Hotazel area (Simondium-3; Fig. 2), ~100 km northwest of the Klipfontein asbestos mine. Stilpnomelane-rich mudrocks intercalated with BIF are interpreted to represent episodic volcanism accompanying the deposition of precursor BIF sediments. The U-Pb zircon age of the stilpnomelane-rich tuffaceous mudstones was thus used to constrain the age of the BIF to 2460 ± 5 Ma (Pickard, 2003). The similarity in age and lithology between the Kuruman Iron Formation and the Brockman Iron Formations in the Hamersley Basin of Western Australia has led to the assumption that these two BIFs either formed on the same continent (e.g., Cheney, 1996; de Kock et al., 2009) or were products of global-scale magmatic events (e.g., Barley et al., 1997). Both are amongst the best-preserved BIFs in the early Precambrian. Thermodynamic calculations of the stability fields of minerals

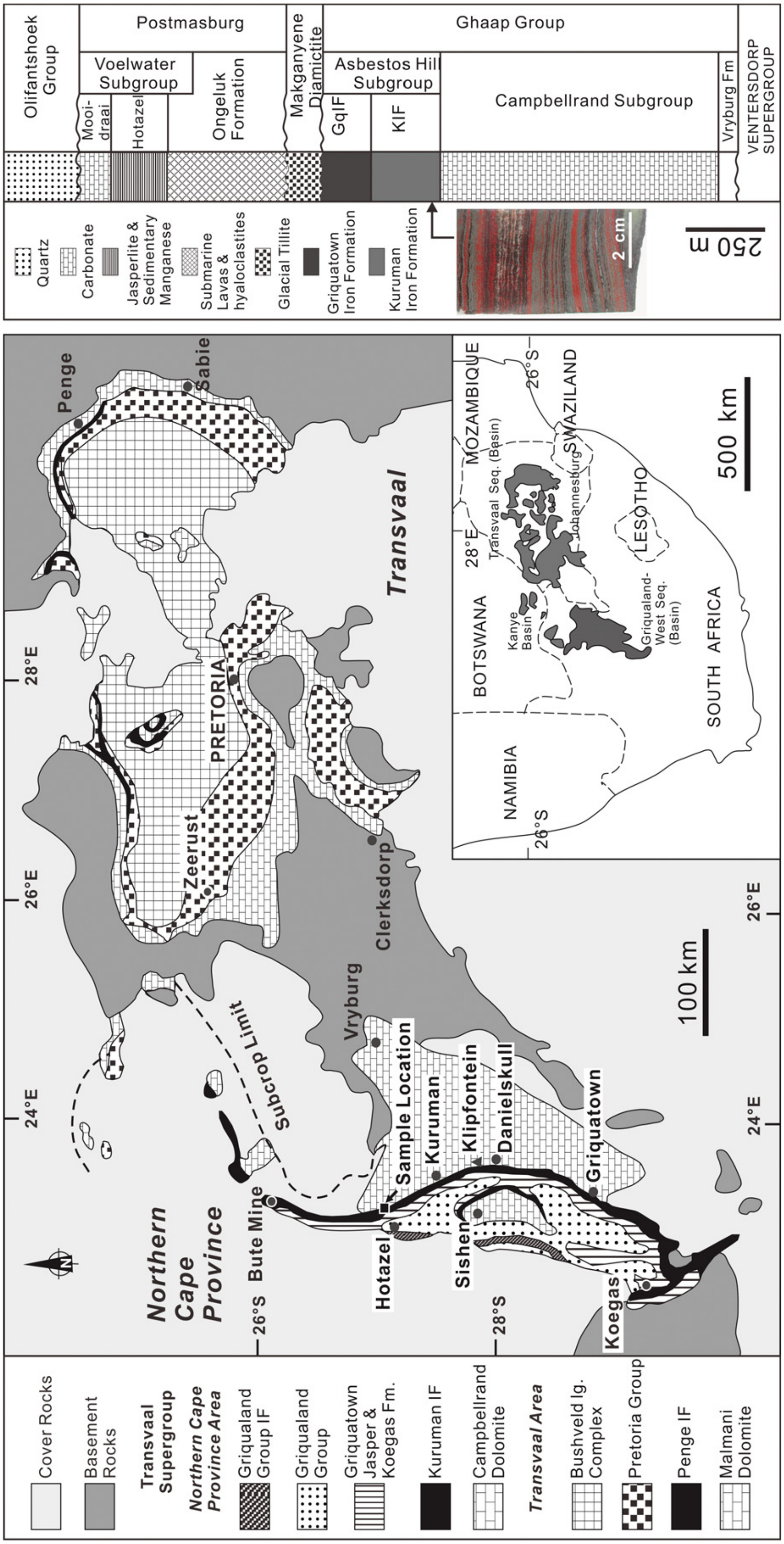

Figure 2. Geology and stratigraphy of the Transvaal Supergroup (after Pickard, 2003). IF—iron formation.

(e.g., riebeckite) in the Kuruman Iron Formation have shown that the BIF did not undergo metamorphic temperatures >170 °C or pressures >1.2 kbar (Miyano and Beukes, 1984).

METHODS

The petrographic data were collected with both an optic microscope (OM) and electron microscopes. The optic microscopy, including transmitted and reflected light imaging of thin sections, is for observations at a relatively larger scale (tens of micrometers to a few millimeters), while the electron microscopy is for observations on delicate textures and mineralogical structures at micro- and even nanoscales. Apart from microscopic observations, energy dispersive X-ray spectroscopy (EDS) and selected area electron diffraction (SAED) methods were applied to determine mineral chemical compositions and crystal structures. Minerals were identified on the basis of their optical properties and EDS and SAED patterns. The electron microscopes used in this study include a Hitachi S-4800 FEG and a Hitachi S-3400N variable-pressure scanning electron microscope (SEM) equipped with EDS detectors (operated at 5 kV and 20 kV) and a FEI Tecnai G2 20 S-Twin scanning transmission electron microscope (STEM; operated at 200 kV) equipped with EDS and SAED systems. Samples for SEM observations were first polished by 120–4000 grit abrasive paper, and then a thin layer on their surface was peeled off to reveal a fresh part for immediate observation.

Based on the OM and SEM results, micro- and nanocrystals were selected for in situ TEM-SAED characterizations. These TEM samples were first mechanically polished to a thickness of a few micrometers and then further milled to be less than 1 µm in thickness by a 4.0 kV argon ion-beam on a GATAN precise ion polishing system. To extract pure hematite from the iron-rich bands, the samples were ground and immersed in ethanol to make a suspension. The upper fraction of the suspension was loaded onto a copper grid for TEM-SAED-EDS analysis.

RESULTS

Petrographic Observations

Both BIFs consist of hematite, chert, magnetite, carbonates (siderite to ferro-dolomite), stilpnomelane, and apatite. Except for apatite, microbands of these minerals were observed, with thicknesses ranging from a few micrometers to a few millimeters (Fig. 3; Li, 2014). The iron- and silica-rich banding structures extend throughout the specimen; they can even extend

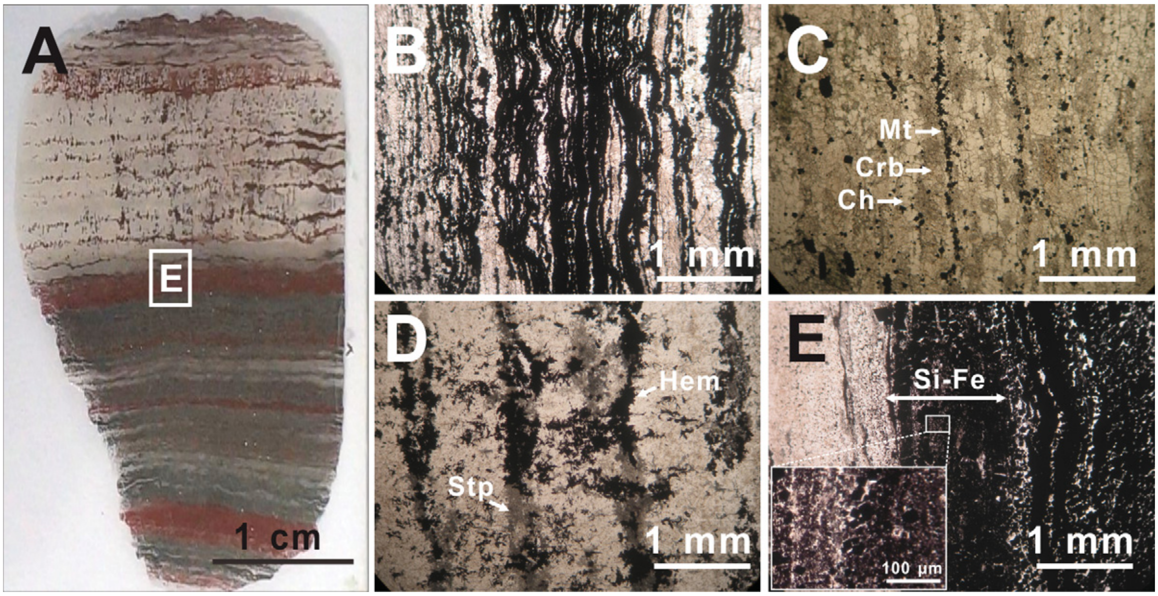

Figure 3. Optic microscopic (OM) images of microbands under transmitted light (TL) from the Kuruman Iron Formation: (A) overview of a thin section, (B) alternating silica- and iron-rich microbands, (C) microbands of carbonates (Crb), chert (Ch), and magnetite (Mt), (D) stilpnomelane (Stp) microbands replaced by hematite (Hem), and (E) transitional band (Si-Fe) between chert- and iron-rich bands marked in A.

kilometers laterally in the field (Morris, 1993). By contrast, the carbonate and stilpnomelane microbands only occur locally as diffusive or discontinuous laminae within the chert matrix. Between the chert- and iron oxide–rich bands, transitional bands made of both chert and iron oxides exist.

Chert is the most abundant phase in both BIFs, appearing either as pure microbands (Figs. 3A and 5A) or as matrix around other minerals. It was also commonly observed as remnants within other minerals, such as ferroan dolomite. Due to diagenesis and/or low-grade metamorphism, the chert in the Abitibi and Kuruman BIFs appears as tightly compacted polyhedrons (Li et al., 2013b).

Hematite in both BIFs exists in three forms. The first consists of aggregates of nanosized particles in the iron oxide–rich bands (H1). The second is made of submicrometer hematite crystals within a chert matrix in what we describe as a “transitional zone” between the iron oxide– and chert-rich bands (H2). The H2 crystals are randomly distributed in the chert rather than having preferential orientation along structures such as fractures or layer boundaries (Figs. 4A–4B). The third is made of needle-like grains showing radial orientations (H3; Figs. 4C–4D). Each hematite needle is tens to hundreds of micrometers in length and ~5 μm in width. Different from H1 and H2, H3 is preferentially aligned along fractures, as well as bands of carbonate or stilpnomelane (Fig. 3D). H3 grains are commonly truncated or were formed as a replacement of stilpnomelane and carbonates (Figs. 4C–4D).

Optical microscopic observations reveal that carbonates in both BIFs commonly occur as micrometer-sized (10–30 μm) particles (Fig. 5B), or anhedral to subhedral crystals that are tens to hundreds of micrometers in size (Fig. 5C). These particles have irregular cores of chert remnants, while the anhedral to subhedral crystals are cut by magnetite. Combined SEM observations under backscattered electron mode (BSE) and EDS results further reveal that the crystals are ferroan dolomite/ankerite with varying Fe/(Mg + Ca) ratios: The bright areas have higher Fe/(Mg + Ca) ratios than the dark areas (Fig. 5D). Disseminated carbonates replacing the chert matrix (Fig. 5E) and remnant carbonate surrounding subhedral to euhedral magnetite crystals (Fig. 5F) were also observed under SEM. Both were rarely observed under the traditional OM due to their small sizes and rare occurrence.

Magnetite appears as large subhedral to euhedral crystals (tens to hundreds of micrometers in size) disseminated within hematite-rich layers or transitional zones (Figs. 4A–4B, 4D, 5B–5D, and 5F–5G), or as crystals aligned to form microbands (tens to hundreds of micrometers in thickness; Figs. 3A–3B, 3E, 5A, and 5C; Li, 2014). Magnetite crystals frequently overgrow other minerals such as stilpnomelane or carbonates.

Stilpnomelane mainly occurs as discontinuous microbands in the matrix of chert, iron oxides, or carbonates. The stilpnomelane crystals show radiating forms and are commonly replaced by H3 or overgrown by magnetite crystals (Fig. 5G).

Apatite is a minor phase in both BIFs. It was only observed under SEM or STEM of high spatial resolutions with generally two forms: one consists of nanosized particles and microscale radial flowers (Li et al., 2013c; Sun et al., 2014); the other is large, euhedral to anhedral crystals of tens to hundreds of micrometers in size (not shown), and these crystals frequently truncate microbands or cut other minerals.

High-Resolution Characterization and SAED Analysis of Hematite

TEM and SAED analysis of hematite in the iron oxide–rich bands (H1) reveals that it consists of aggregates made of numerous 3–5-nm-sized ultrafine hematite nanocrystals. Figure 6A is a fragment of H1, ~200 nm in size, along with its SAED pattern (inset of Fig. 6A). The SAED pattern shows several diffraction rings matching (hkl) indexes of (104), (110), (113), (202), and (116) of hematite in the X-ray powder diffraction database (PDF86–0550; Table 1). High-resolution TEM observations of this fragment demonstrate that it is made of numerous 3–5 nm lattice fringe domains, each of which represents

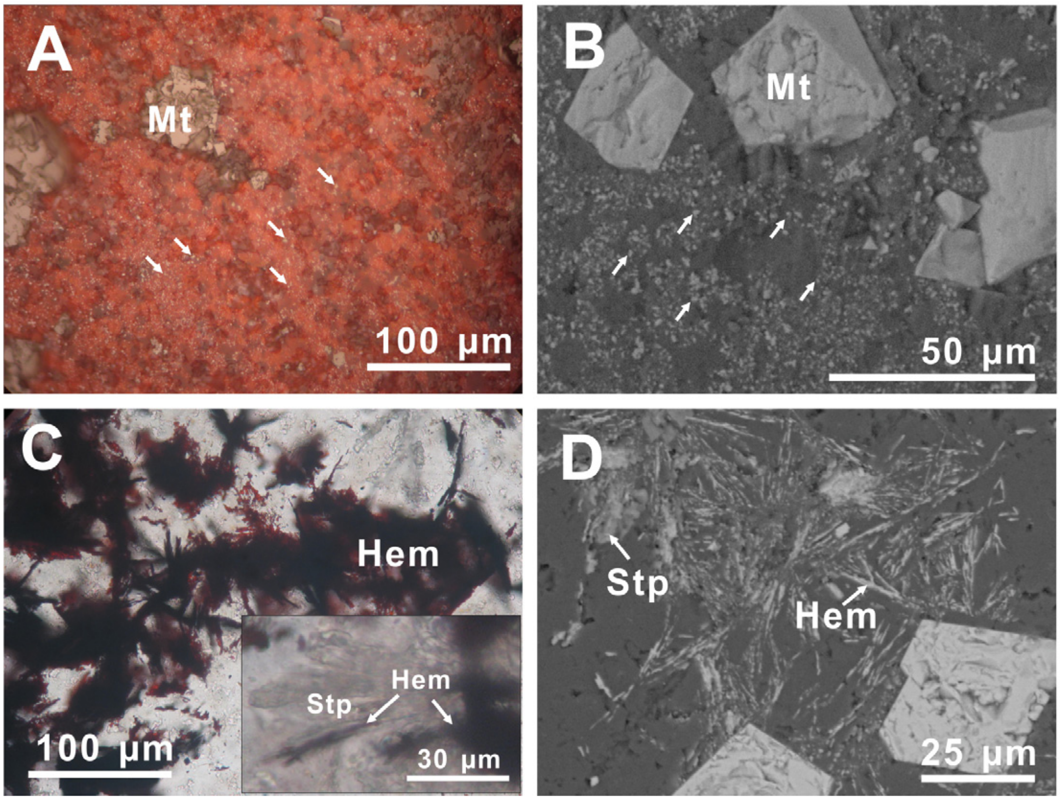

Figure 4. Optic microscopic (OM) and scanning electron microscopic (SEM) images of petrographic features of hematite (Hem) from the Kuruman Iron Formation. (A) Reflected light (RL) image of submicrometer hematite crystals (H2) as evident by bright dots with arrows scattered amongst the chert matrix. (B) SEM image of H2 (bright dots with arrows) under backscattered electron (BSE) mode. (C) Transmitted light (TL) image of H3, with inset showing a stilpnomelane (Stp) crystal replaced by H3. (D) SEM-BSE image of needle-like H3 replacing stilpnomelane crystals. Mt—magnetite.

one nanocrystal. The 3–5 nm lattice fringes are further confirmed to be hematite by having 3.7 and 2.7 Å *d*-spaces corresponding to (012) and (104) of hematite (Fig. 6B). The fast Fourier transform (FFT) yielded the same result (inset in Fig. 6B).

Hematite crystals in the transitional zones (H2) have mineralogical features distinct from H1. High-resolution SEM observations show that the H2 crystals are randomly distributed within the chert matrix, without any preferential direction such as layering planes or fractures. They are scattered monocrystals ranging from 100 to 800 nm in diameter (500 ± 300 nm in average), with subhedral to euhedral morphologies (e.g., rhombohedra; Figs. 7A–7B). Nanoscale dislocations or fractures are widely observed in chert, forming networks or trails connecting to these hematite crystals (Fig. 7D). Some of the fractures are pinned with tiny “strained” bubble structures that represent the previous presence of water (Fig. 7D; e.g., Meng et al., 2009). Such dislocations and fractures are potential pathways for structural water to percolate within the chert (Bakker and Jansen, 1990). Chemically, only elements Fe and O were detected by EDS in these fine particles, indicating their pure iron-oxide compositions. Forty particles with various morphologies were analyzed by SAED. They all yielded regular spot arrays matching diffraction patterns of hematite monocrystals (Figs. 7E–7F).

Under high-resolution TEM, most H2 crystals display clean surfaces and homogeneous interiors, while the remainder contain a number of finer euhedral hematite crystals, ~20–30 nm in size. For example, in one hematite crystal of ~800 nm in size (Fig. 8A), there are a few euhedral nanosized crystals, the crystal faces of which are delineated by the straight boundaries of the lattice fringe domains (Fig. 8B). The SAED pattern of this euhedral hematite crystal yields bright regular spot arrays matching hematite monocrystal from the zone axis (–4,–8,1) (Fig. 8C). In addition to the bright regular spots, there are dimmer spots as well in the background, making weak but discernible circles overlapping some of the bright spots belonging to the diffraction pattern of the large hematite monocrystal (Fig. 8C). The *d*-space represented by the innermost circle is 2.66 Å, corresponding to (104) of hematite. Similar hematite particles of 20–30 nm in size are also observed in chert surrounding the subhedral to euhedral hematite (Figs. 8D–8E). The SAED of their aggregates yields several rings representing (hkl) indexes of (104), (110), (113), (202), (018), (208), and (134) of hematite in the X-ray powder diffraction database (PDF86–0550; Fig. 8F; Table 1).

DISCUSSION

Mineral Paragenesis

According to the petrographic observations, a mineral paragenetic sequence can be deduced for both BIFs. The earliest mineral phases preserved are (1) chert, (2) hematite in the iron oxide–rich microbands (H1), and (3) submicrometer hematite (H2) in the chert matrix of Fe-Si transition zones. Replacement of the chert matrix by carbonate and the chert remnants in the center of the carbonate granules suggest that carbonate formed later than the chert. Both carbonates and stilpnomelane appearing as discontinuous microbands in the chert matrix have been interpreted as having formed during diagenesis to low-grade metamorphism (Li, 2014). Similar overprinting patterns of the original sediments were also reported in the Dales Gorge Member (Li, 2014). The preferential distribution of H3 along the fractures and carbonate/stilpnomelane microbands, and the truncation and/or replacement structures of carbonate and stilpnomelane by H3 collectively imply that H3 hematite postdates both carbonate and stilpnomelane. This hematite was probably formed by some fluid-mediated processes during or after diagenesis-metamorphism, and thus it has a similar genesis as that from the Dales

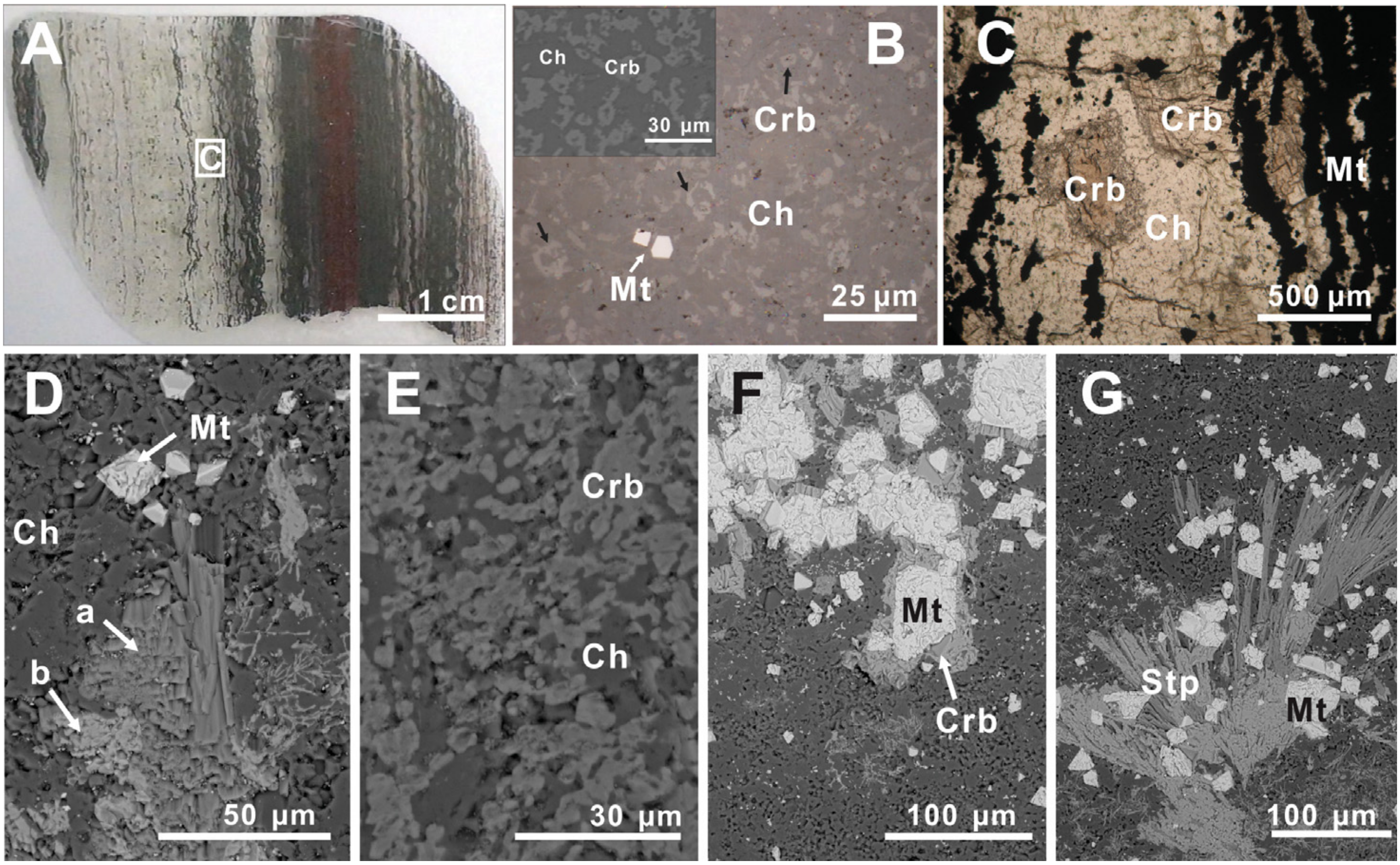

Figure 5. Optic microscopic (OM) and scanning electron microscopic (SEM) images of petrographic features of minerals in the Kuruman Iron Formation. (A) Overview of a thin section. (B) Reflected light (RL) and backscattered electron (BSE; inset) image of carbonate (Crb) micrograins (e.g., see black arrows) with irregular chert (Ch) remnants in their centers. (C) Transmitted light (TL) image of large (hundreds of micrometers in diameter) carbonate crystals crosscut by magnetite (Mt). (D) BSE image of carbonate crystals with varying Fe/(Mg + Ca) ratios; "a" has lower Fe/(Mg + Ca) ratio than "b". (E) BSE image of carbonates (light regions) replacing chert matrix (dark regions). (F) BSE image of carbonate remnant surrounding euhedral magnetite crystals. (G) BSE image of magnetite crystals developing over stilpnomelane (Stp).

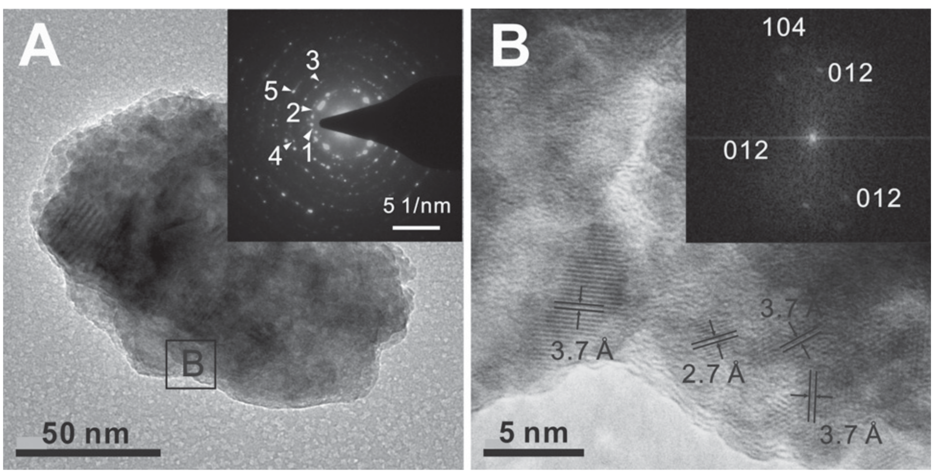

Figure 6. Transmission electron microscopic (TEM) images and selected area electron diffraction (SAED) patterns of hematite from iron-oxide bands (H1) in the Kuruman Iron Formation. (A) TEM image and SAED pattern (inset) of one hematite aggregate of ~200 nm in size. (B) High-resolution TEM characterization of H1 showing nanodomains (3–5 nm in sizes) of lattice fringes and fast Fourier transform results (inset); each lattice fringe domain represents one crystal.

TABLE 1. SELECTED AREA ELECTRON DIFFRACTION DATA OF THE ULTRAFINE HEMATITE PARTICLES FROM IRON OXIDE–RICH BANDS AND HEMATITE FINE PARTICLES IN THE CHERT OF THE TRANSITION ZONES

	d-spaces (Å)			
Diffraction rings	PDF86-0550	Ultrafine hematite in iron-oxide bands*	Hematite in chert of transitional bands†	(hkl)
1	2.699	2.688	2.667	104
2	2.518	2.550	2.569	110
3	2.207	2.202	2.208	113
4	2.078	1.966	1.929	202
5	1.695	1.682	1.610	116
6	1.350	N.A.§	1.357	208
7	1.140	N.A.	1.140	134

*Ultrafine particles in iron-rich bands (see Fig. 6A).
†Fine particles (20–30 nm) in the quartz of transition zones (Fig. 8F).
§N.A.—not applicable.

Gorge BIF (Rasmussen et al., 2014) or hematitic ores (e.g., Morris, 1980; Taylor et al., 2001; Rasmussen et al., 2007; Beukes et al., 2008).

The euhedral magnetite crystals of tens to a few hundreds of micrometers in size formed even later, since they grow over nearly all other minerals and even form microbands that obscure the original hematite bands. Carbonate remnants surrounding the subhedral to euhedral magnetite crystals (Fig. 5E) imply that the magnetite crystals might have grown larger at the expense of carbonate ($3FeCO_3 + H_2O \rightarrow Fe_3O_4 + 3CO_2 + H_2$) under high temperatures (>230 °C; Kaufman et al., 1990). Alternatively, both carbonate and magnetite could have formed from older Fe(III) minerals (e.g., ferrihydrite) through Fe(III) reduction coupled to the oxidation of buried organic matter (e.g., microbial cell biomass) during diagenesis to low-grade metamorphisms at temperatures up to 250 °C (e.g., Viswanathiah et al., 1980; Koehler et al., 2013; Li et al., 2013a; Posth et al., 2013a, 2013b). In this case, the magnetite and carbonate may have a similar age (Li, 2014). This observation is consistent with the experimental study in which magnetite crystals in BIFs were interpreted to form by three steps: beginning with Fe(III) reduction of initial ferric iron–rich sediment coupled to the oxidation of the decayed phytoplankton, followed by magnetite crystal aging, and ultimately pressure-temperature–induced abiotic enlargement of the biogenic magnetite during metamorphism (Li et al., 2013a). Apatite crystals of tens to hundreds of micrometers in size belong to the youngest minerals formed. They are reminiscent of similar apatites from the ca. 3.8 Ga Akilia and Isua supracrustal rocks, West Greenland, which have a metamorphic origin (Lepland et al., 2002; Nutman and Friend, 2006).

Formation of Hematite

Based on the high-resolution electron microscopic analyses, we infer that the ultrafine hematite particles in H1 are similar to those making up the hematite nanospheres from the ca. 2.5 Ga Marra Mamba BIF of Hamersley, Australia, which formed through dehydration of a precursor ferrihydrite phase during early diagenesis (Ahn and Buseck, 1990). The absence of recrystallization is robust evidence that they are well preserved despite later-stage fluid alterations and modern weathering processes.

For submicrometer hematite crystals (H2), we suggest that they are also "primary" (where the word "primary" used here refers to the ferric iron inherited from the original minerals precipitated from seawaters; they are not necessarily the original minerals themselves) for the following reasons: (1) They are randomly scattered within the chert matrix rather than showing preferential distributions, such as within fractures or band boundary surfaces; (2) they only appear in transition zones between the iron oxide– and chert-rich bands, indicating that they formed in a continuously changing environment rather than in later-stage fluid channels; and (3) they have contrasting features to the "secondary" hematite, which is usually closely related to other iron-bearing minerals, for example, microplaty hematite coexisting with goethite and radial/colloform hematite on the surface of magnetite (Morris, 1993, 2012). These features are more reminiscent of H3 reported here, and the grains replacing stilpnomelane (Rasmussen et al., 2014). We suggest that the H2 crystals are also dehydration products of ferric oxyhydroxide precursors, but they differ from H1 by having undergone a coarsening process. The 20–30 nm fine particles are relics of the intermediate phase during coarsening. The coarsening process might have been promoted by the surrounding chert, which not only clustered the hematite fine particles (Cornell et al., 1987), but also released water from its structure during amorphous silica to quartz transformation (e.g., Frondel, 1982; Meng et al., 2009). The structural water in chert could have been preserved for a long geological time (e.g., Frondel, 1982; Meng et al., 2009). Mobilization of the structural water during diagenesis or low-grade metamorphism facilitates the coarsening of the ultrafine hematite crystals via Ostwald ripening in which competitive growth takes place through dissolution and subsequent recrystallization (Morse and Casey, 1988). The trails and dislocations (Figs. 4C–4D) connecting the hematite crystals in chert are likely such paths for water to reach the iron minerals. In contrast to the H2 crystals in the chert matrix, H1 in the iron-rich bands lacked internal water, so that it remains ultrafine.

Implications for the Depositional Model of BIFs

To understand the depositional processes underpinning the genesis of BIFs, it is essential to discern their original mineral compositions. Ferric oxyhydroxides, such as ferrihydrite, have previously been suggested as original minerals precipitated from the oceanic water column (e.g., Ahn and Buseck, 1990; Konhauser et al., 2002, 2007). However, it has also been suggested instead that iron-silica microgranules were the primary precipitates (Rasmussen et al., 2013, 2014). In our samples, the widespread occurrence of primary hematite (H1 and H2) demonstrates that at least part of the hematite in Neoarchean to Paleoproterozoic BIFs is primary, and this implies ferrihydrite could be a precursor mineral. Besides ferrihydrite, amorphous silica, siderite, and Fe-rich/Al-poor silicates {e.g., greenalite [$(Fe^{2+},Fe^{3+})_{2-3}Si_2O_5(OH)_4$], chamosite [$(Fe^{2+},Mg,Fe^{3+})_5Al(Si_3Al)O_{10}(OH,O)_8$], or nontronite [$(Na,K,0.5Ca)_{0.3}Fe_2(Si,Al)_4O_{10}(OH)_2n(H_2O)$]} are also considered as candidates of original minerals, with the silica and siderite being the precursor of chert/quartz and ferroan dolomite, respectively, and the other minerals having transformed to stilpnomelane (Klein, 2005; Bekker et al., 2014).

The existence of ferric oxyhydroxide as a precursor mineral indicates that, in the anoxic, ferruginous ocean in which BIFs were deposited, Fe(II) oxidation did take place (Posth et al., 2014). It has been proposed that Fe(II) was either oxidized enzymatically by phototrophic Fe(II)-oxidizing bacteria (e.g., Widdel et al., 1993; Konhauser et al., 2002; Hegler et al., 2008; Wu et al., 2014) or abiotically by cyanobacteria-produced oxygen (e.g., Konhauser et al., 2002, 2007). The pervasive distribution of alternating silica- and iron oxide–rich bands in BIFs reflects a background condition in which seawater was saturated with silica or iron that was likely hydrothermally sourced (Bekker et al., 2014). Ferrihydrite-rich sediment layers formed when the supply or the oxidization rate of Fe(II) overwhelmed the precipitation rate of silica due

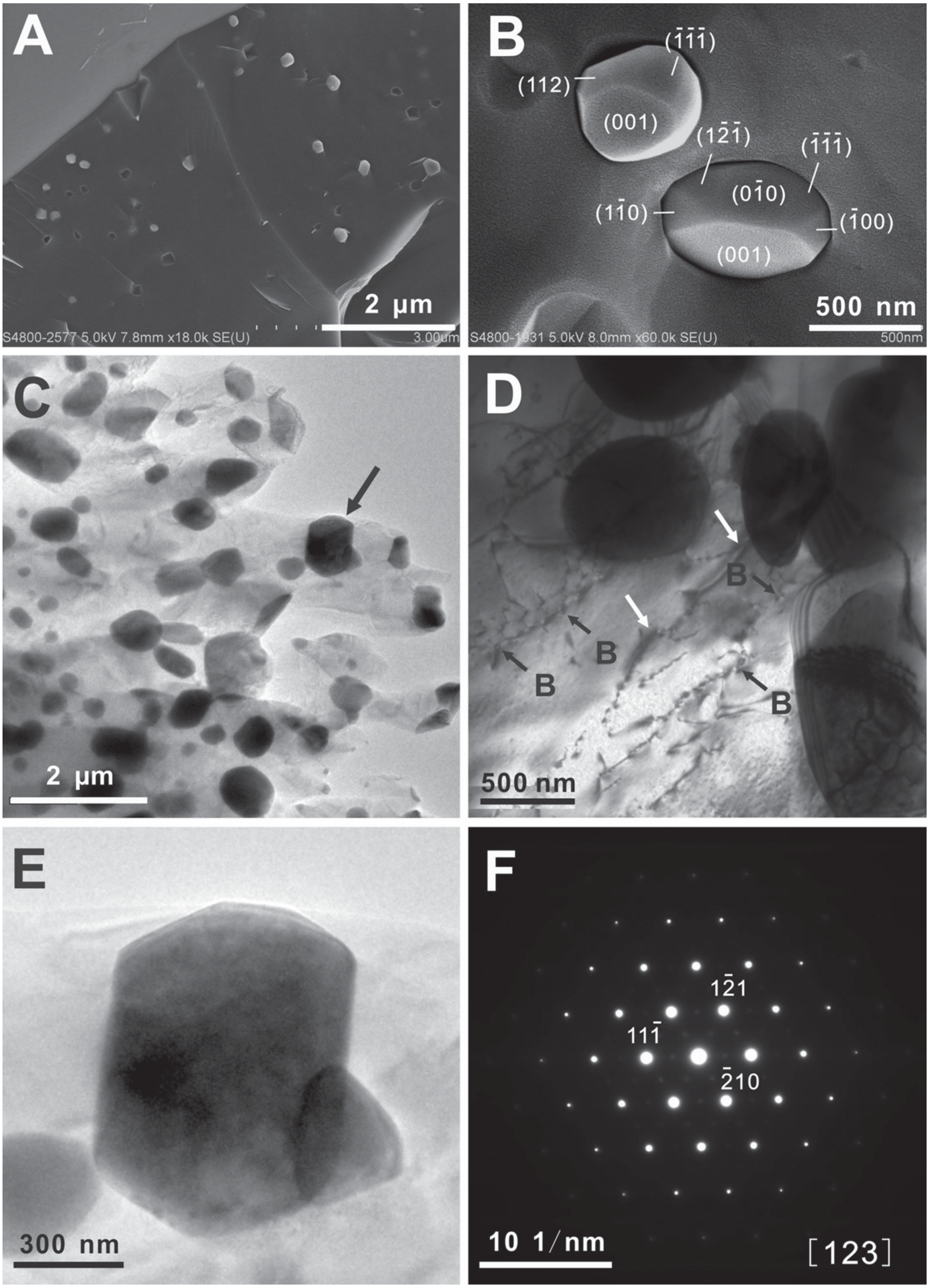

Figure 7. Scanning electron microscopic (SEM) and transmission electron microscopic (TEM) images, and selected area electron diffraction (SAED) patterns of submicrometer hematite crystals from the transitional zones (H2). Images A, C, and E are from the Abitibi banded iron formation, while images B, D, and F are from Kuruman Iron Formation. (A–B) SEM images of H2 under secondary electron mode (SE). (C–D) TEM images of H2 showing dislocations connecting them (white arrows) and "strained" bubbles structures (black arrows with "B"). (E) Magnified image of the arrowed hematite crystals in C. (F) SAED pattern of one hematite crystal.

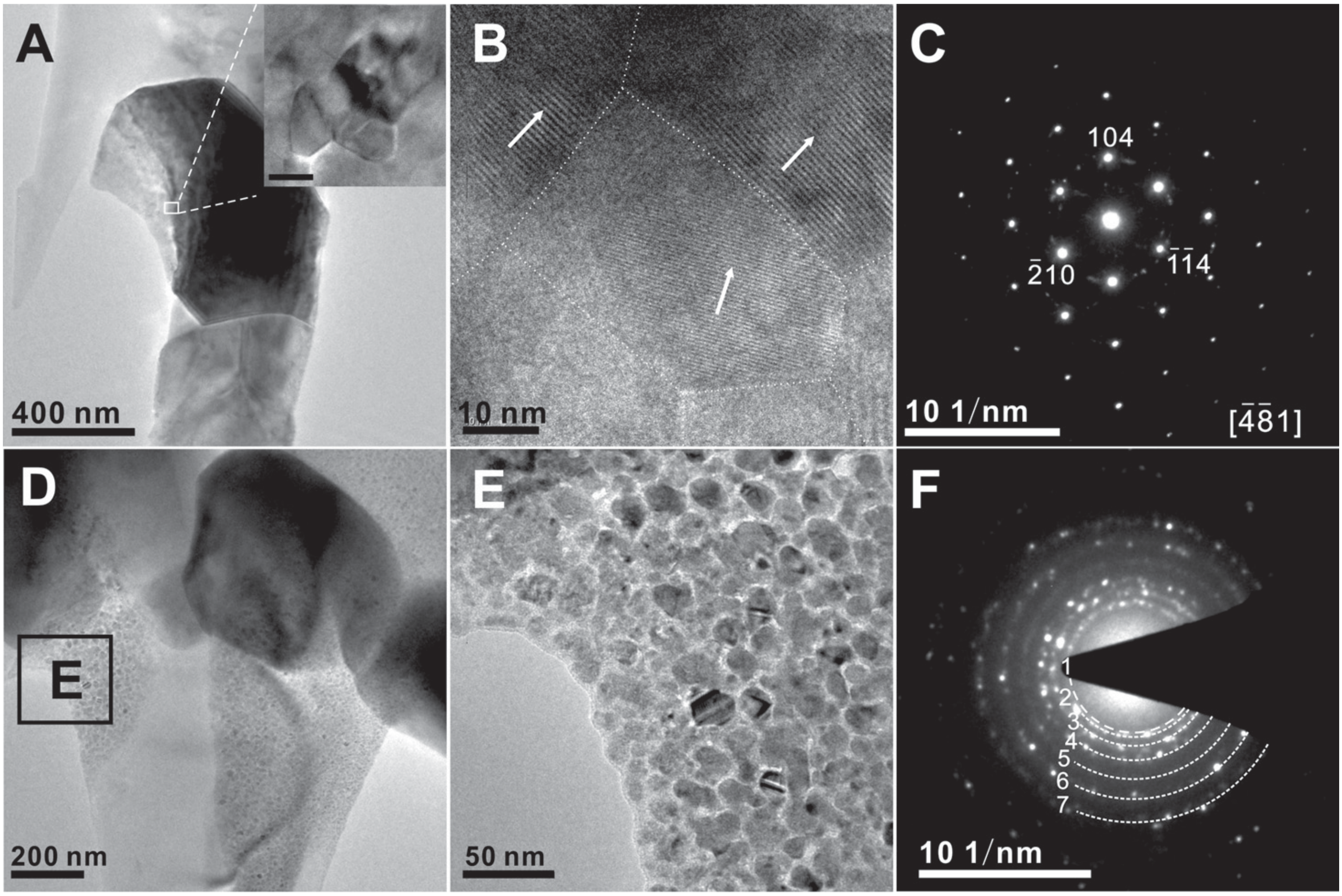

Figure 8. High-resolution transmission electron microscopic (TEM) images and selected area electron diffraction (SAED) patterns of submicrometer hematite crystals (H2) from the Kuruman Iron Formation. (A) TEM image of an H2 crystal containing 20–30 nm fine hematite crystals. (B) High-resolution TEM image of the fine particles in one H2 crystals, showing lattice fringes of different hematite crystals in the 20–30 nm size range; the 20–30 nm crystals are delineated by the straight boundaries of the lattice. (C) SAED pattern of the hematite crystal in A. Bright regular spot arrays and dimmer spots appear in the pattern. The dimmer spots make up weak but discernible circles overlapping some of the bright spots. (D) TEM image of the 20–30 nm hematite crystals in the chert surrounding H2 crystals. (E) Magnified image of the squared area in D. (F) SAED pattern of the fine hematite particles in E.

to seasonal cycling or temperature fluctuations (e.g., Holland, 1973; Morris, 1993; Posth et al., 2008), while silica-rich layers formed at times when Fe(II) oxidation was not favored. Biomass deposited along with silica and ferric iron onto the seafloor was buried as a source of easily oxidizable organic carbon. Concomitantly, episodic variations in seawater geochemistry (e.g., pH, Eh, temperature, solutes), fluctuations in hydrothermal fluxes, or changes in magma chamber activities led to considerable deposition of minerals other than silica and ferric (oxy)hydroxides (e.g., siderite and greenalite; Klein, 2005; Bekker et al., 2014). For instance, increased supply of dissolved inorganic carbon (Bolhar et al., 2005) coupled with decreased pH (lower than 7; Harder, 1978) caused by enhanced submarine volcanic activities may have facilitated considerable precipitation of siderites and Fe-rich silicates (e.g., Konhauser et al., 2007).

After the deposition of precursor minerals, diagenesis and/or low-grade metamorphism transformed the primary iron oxyhydroxides to more stable phases, such as hematite (Koehler et al., 2013; Posth et al., 2013a, 2013b). In the presence of Fe(II), ferrihydrite to hematite transformation could be promoted in a solid state (Liu et al., 2005). The structural water of chert is much more resistant to temperature and pressure increases than the water associated with ferric oxyhydroxides, so that it could be preserved even to the later stages of diagenesis or low-grade metamorphism. As the sediments underwent increased temperature- and pressure-induced changes during burial, water mobilized from the chert facilitated the coarsening of the ultrafine hematite particles in it (Fig. 9). In contrast, hematite particles in the iron oxide–rich bands remained ultrafine due to the lack of water. With increased temperature and pressure, the buried organic matter (biomass) was oxidized coupled with the reduction of Fe(III) to Fe(II) (Koehler et al., 2013; Posth et al., 2013a, 2013b). This process supplied Fe(II) for the formation and coarsening of the large euhedral magnetite crystals, and perhaps some of the Fe(II)-containing silicates as well (e.g., Walker, 1984; Konhauser et al., 2005; Li et al., 2013a). In terms of siderite, Mg and Ca from pore waters or much later secondary fluids could have replaced part of the Fe(II), forming ferroan dolomite with varied Fe/(Mg + Ca) ratios. The external fluids introduced through fractures or layer boundaries could remobilize elements in

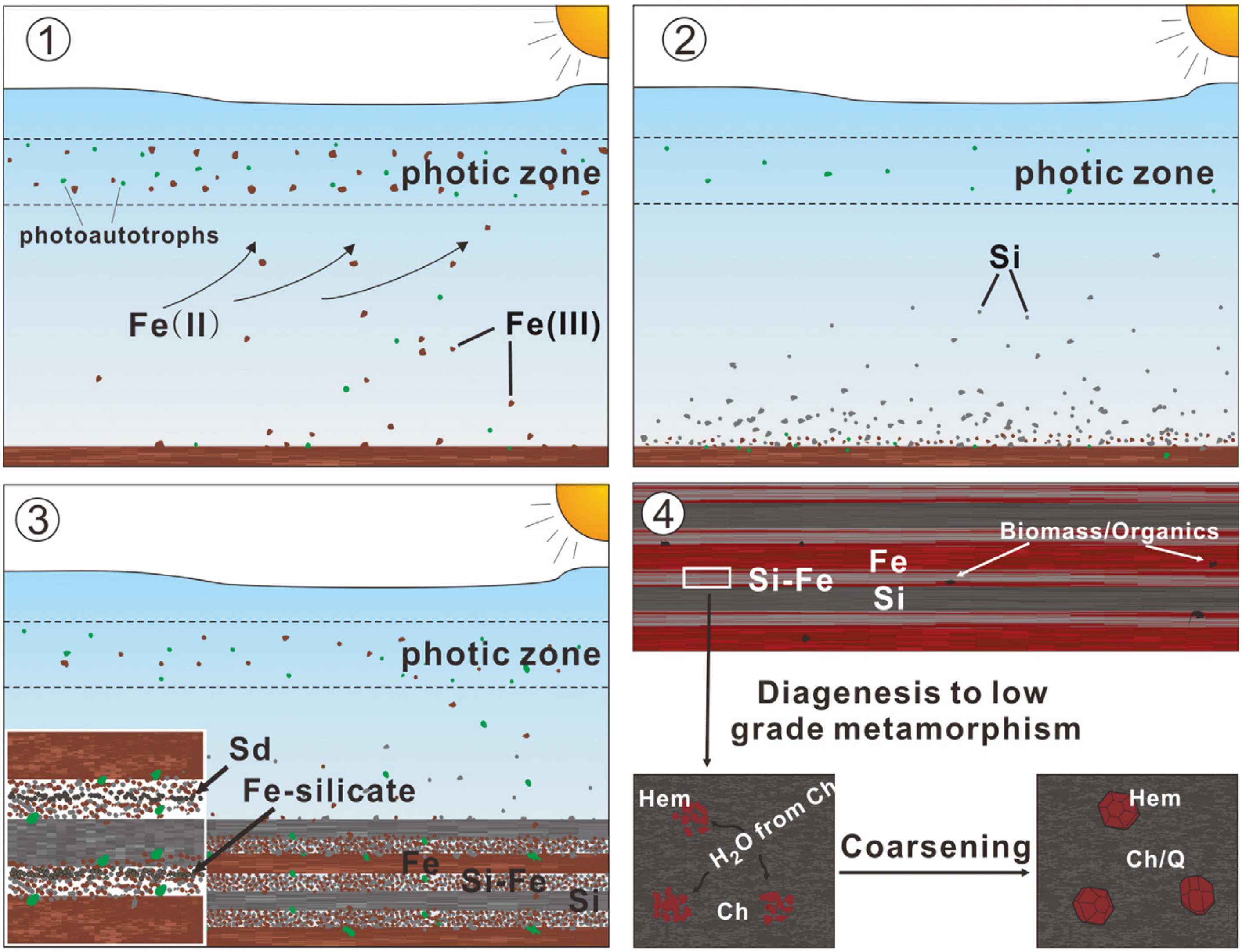

Figure 9. Schematic diagrams of the depositional model of banded iron formation and the formation of hematite. (1) The precipitation of ferrihydrite via biological or abiological Fe(II) oxidization overwhelms silica deposition, leading to the iron oxide–rich bands. (2) Due to the decreasing supply of dissolved Fe(II) and/or a temperature-related slowing down in biological oxidation rates of Fe(II), coupled with increasing precipitation rate of silica, there is a transition from iron oxide–rich bands to silica-rich bands. (3) Intermittent changes in geochemical or physical conditions cause episodic deposition of minerals other than ferrihydrite and amorphous silica, e.g., siderite (Sd) and greenalite (Fe-silicate) in the inset. (4) During diagenesis to low-grade metamorphism, the ferric oxyhydroxides in the iron-rich bands are dehydrated to hematite and remained ultrafine (H1), while those in the chert matrix of the transition zones grow larger (i.e., H2) with the aid of water released during amorphous silica to quartz (Q) transformation. The bands marked "Si," "Si-Fe," and "Fe" refer to silica-rich bands, silica-iron transitional bands, and iron-rich bands, respectively. Hem—hematite; Ch—chert, Q—quartz.

the primary sediments, leading to the formation of secondary minerals via recrystallization or replacement, such as H3 and similar hematite in hematite-rich ores (e.g., Morris, 1980; Taylor et al., 2001; Rasmussen et al., 2007; Beukes et al., 2008). The source of ferric iron in H3 is unclear. It could either have been inherited from the Fe(III)-bearing precursors, or it might have come from the Fe(II)-containing silicates oxidized by oxic fluids introduced much later in time (Rasmussen et al., 2013, 2014).

CONCLUSIONS

Based on detailed petrographic observation, high-resolution TEM characterization, and mineral structural analysis by SAED, three types of hematite are identified in the 2728 Ma BIF from the Abitibi greenstone belt located in the Superior Province in the Canadian Shield and the 2460 Ma Kuruman Iron Formation in South Africa: (1) hematite comprising 3–5 nm nanocrystals in the iron oxide–rich bands (H1), (2) submicrometer subhedral to euhedral hematite crystals randomly distributed in transition zones between the silica- and iron oxide–rich bands (H2), and (3) needle-like, fibrous or radial hematite replacing stilpnomelane or carbonate, and distributed along the fractures or microbands of carbonate and stilpnomelane (H3). The first two types of hematite were inherited from primary ferric iron precipitates (e.g., ferrihydrite) and were mineralized during early diagenesis of the BIF via dehydration. H1 is similar to the hematite nanocrystals forming the microspheres in the ca. 2.5 Ga Marra Mamba Banded Iron Formation of Hamersley, Australia. H2 underwent a coarsening process facilitated by internal fluids mobilized during the transformation of the initial amorphous silica to quartz. H3 is a secondary mineral that formed during a late-stage, fluid-mediated replacement of carbonate and iron-containing silicates. The identification of both primary and secondary hematite in the studied BIFs suggests that at least part of the hematite inherited ferric iron from initial ferric oxyhydroxides, and, therefore, Fe(II) oxidation, via either a biotic or abiotic mechanism, did occur in the overlying seawater from which the BIFs were deposited.

ACKNOWLEDGMENTS

We thank Axel Hofmann from the University of Johannesburg for providing the core sample of the Kuruman Iron Formation and Christopher Fedo from the University of Tennessee for providing the sample from the Abitibi greenstone belt. We also thank the two reviewers (Andrey Bekker and an anonymous reviewer) for their reviews and constructive scientific comments, Editor David Ian Schofield and Associate Editor Rob Rainbird for processing our manuscript and for their suggestions on science and language as well. Y.-L. Li was supported by the Research Grants Council of Hong Kong (HKU703412P). K. Konhauser was supported by the Natural Sciences and Engineering Research Council of Canada (NSERC). A. Kappler was supported by the German Research Foundation (DFG; KA 1736/24-1).

REFERENCES CITED

Ahn, J.H., and Buseck, P.R., 1990, Hematite nanospheres of possible colloidal origin from a Precambrian banded iron formation. Science, v. 250, p. 111–113, doi:10.1126/science.250.4977.111.

Bakker, R.J., and Jansen, J.B.H., 1990, Preferential water leakage from fluid inclusions by means of mobile dislocations. Nature, v. 345, p. 58–60, doi:10.1038/345058a0.

Barley, M.E., Pickard, A.L., and Sylvester, P.J., 1997, Emplacement of a large igneous province as a possible cause of banded iron formation 2.45 billion years ago. Nature, v. 385, p. 55–58, doi:10.1038/385055a0.

Bekker, A., Slack, J.F., Planavsky, N., Krapež, B., Hofmann, A., Konhauser, K.O., and Rouxel, O.J., 2010, Iron formation: The sedimentary product of a complex interplay among mantle, tectonic, oceanic, and biospheric processes. Economic Geology and the Bulletin of the Society of Economic Geologists, v. 105, p. 467–508, doi:10.2113/gsecongeo.105.3.467.

Bekker, A., Planavsky, N.J., Krapež, B., Rasmussen, B., Hofmann, A., Slack, J.F., Rouxel, O.J., and Konhauser, K.O., 2014, Iron formations: Their origins and implications for ancient seawater chemistry, *in* Holland, H.D., and Turekian, K.K., eds., Treatise on Geochemistry (2nd ed.). Oxford, UK, Elsevier, p. 561–628.

Beukes, N.J., 1984, Sedimentology of the Kuruman and Griquatown Iron Formations, Transvaal Supergroup, Griqualand West, South Africa. Precambrian Research, v. 24, p. 47–84, doi:10.1016/0301-9268(84)90069-X.

Beukes, N.J., and Klein, C., 1990, Geochemistry and sedimentology of a facies transition—from microbanded to granular iron-formation—in the early Proterozoic Transvaal Supergroup, South Africa. Precambrian Research, v. 47, p. 99–139, doi:10.1016/0301-9268(90)90033-M.

Beukes, N.J., Mukhopadhyay, J., and Gutzmer, J., 2008, Genesis of high-grade iron ores of the Archean iron ore group around Noamundi, India. Economic Geology and the Bulletin of the Society of Economic Geologists, v. 103, p. 365–386, doi:10.2113/gsecongeo.103.2.365.

Bolhar, R., Van Kranendonk, M.J., and Kamber, B.S., 2005, A trace element study of siderite–jasper banded iron formation in the 3.45 Ga Warrawoona Group, Pilbara craton—Formation from hydrothermal fluids and shallow seawater. Precambrian Research, v. 137, p. 93–114, doi:10.1016/j.precamres.2005.02.001.

Cheney, E.S., 1996, Sequence stratigraphy and plate tectonic significance of the Transvaal succession of southern Africa and its equivalent in Western Australia. Precambrian Research, v. 79, p. 3–24, doi:10.1016/0301-9268(95)00085-2.

Chown, E.H., Daigneault, R., Mueller, W., and Mortensen, J.K., 1992, Tectonic evolution of the northern volcanic zone, Abitibi belt, Quebec. Canadian Journal of Earth Sciences, v. 29, p. 2211–2225, doi:10.1139/e92-175.

Chown, E.H., N'dah, E., and Mueller, W.U., 2000, The relation between iron-formation and low temperature hydrothermal alteration in an Archean volcanic environment. Precambrian Research, v. 101, p. 263–275, doi:10.1016/S0301-9268(99)00091-1.

Cornell, R.M., Giovanoli, R., and Schindler, P.W., 1987, Effect of silicate species on the transformation of ferrihydrite into goethite and hematite in alkaline media. Clays and Clay Minerals, v. 35, p. 21–28, doi:10.1346/CCMN.1987.0350103.

de Kock, M.O., Evans, D.A.D., and Beukes, N.J., 2009, Validating the existence of Vaalbara in the Neoarchean. Precambrian Research, v. 174, p. 145–154, doi:10.1016/j.precamres.2009.07.002.

Fischer, W.W., and Knoll, A.H., 2009, An iron shuttle for deepwater silica in Late Archean and early Paleoproterozoic iron formation. Geological Society of America Bulletin, v. 121, p. 222–235, doi:10.1130/b26328.1.

Frondel, C., 1982, Structural hydroxyl in chalcedony (type B quartz). The American Mineralogist, v. 67, p. 1248–1257.

Harder, H., 1978, Synthesis of iron layer silicate minerals under natural conditions. Clays and Clay Minerals, v. 26, p. 65–72, doi:10.1346/CCMN.1978.0260108.

Hegler, F., Posth, N.R., Jiang, J., and Kappler, A., 2008, Physiology of phototrophic iron(II)-oxidizing bacteria: Implications for modern and ancient environments. FEMS Microbiology Ecology, v. 66, p. 250–260, doi:10.1111/j.1574-6941.2008.00592.x.

Holland, H.D., 1973, The oceans: A possible source of iron in iron-formations. Economic Geology and the Bulletin of the Society of Economic Geologists, v. 68, p. 1169–1172, doi:10.2113/gsecongeo.68.7.1169.

Kappler, A., Pasquero, C., Konhauser, K.O., and Newman, D.K., 2005, Deposition of banded iron formations by anoxygenic phototrophic Fe(II)-oxidizing bacteria. Geology, v. 33, p. 865–868, doi:10.1130/G21658.1.

Kaufman, A.J., Hayes, J.M., and Klein, C., 1990, Primary and diagenetic controls of isotopic compositions of iron-formation carbonates. Geochimica et Cosmochimica Acta, v. 54, no. 12, p. 3461–3473, doi:10.1016/0016-7037(90)90298-Y.

Klein, C., 2005, Some Precambrian banded iron-formations (BIFs) from around the world: Their age, geologic setting, mineralogy, metamorphism, geochemistry, and origins. The American Mineralogist, v. 90, p. 1473–1499, doi:10.2138/am.2005.1871.

Klein, C., and Beukes, N.J., 1992, Time distribution, stratigraphy, sedimentologic setting, and geochemistry of Precambrian iron-formations, *in* Schopf, J.W., and Klein, C., eds., The Proterozoic Biosphere: A Multidisciplinary Study. Cambridge, UK, Cambridge University Press, p. 139–146.

Koehler, I., Konhauser, K.O., Papineau, D., Bekker, A., and Kappler, A., 2013, Biological carbon precursor to diagenetic siderite with spherical structures in iron formations. Nature Communications, v. 4, p. 1741, doi:10.1038/ncomms2770.

Konhauser, K.O., Hamade, T., Raiswell, R., Morris, R.C., Ferris, F.G., Southam, G., and Canfield, D.E., 2002, Could bacteria have formed the Precambrian banded iron formations? Geology, v. 30, p. 1079–1082, doi:10.1130/0091-7613(2002)030<1079:cbhftp>2.0.co;2.

Konhauser, K.O., Newman, D.K., and Kappler, A., 2005, The potential significance of microbial Fe(III) reduction during deposition of Precambrian banded iron formations. Geobiology, v. 3, p. 167–177, doi:10.1111/j.1472-4669.2005.00055.x.

Konhauser, K.O., Amskold, L., Lalonde, S.V., Posth, N.R., Kappler, A., and Anbar, A., 2007, Decoupling photochemical Fe(II) oxidation from shallow-water BIF deposition. Earth and Planetary Science Letters, v. 258, p. 87–100, doi:10.1016/j.epsl.2007.03.026.

Krapež, B., Barley, M.E., and Pickard, A.L., 2003, Hydrothermal and resedimented origins of the precursor sediments to banded iron formations: Sedimentological evidence from the early Palaeoproterozoic Brockman Supersequence of Western Australia. Sedimentology, v. 50, p. 979–1011, doi:10.1046/j.1365-3091.2003.00594.x.

Lepland, A., Arrhenius, G., and Cornell, D., 2002, Apatite in early Archean Isua supracrustal rocks, southern West Greenland: Its origin, association with graphite and potential as a biomarker. Precambrian Research, v. 118, p. 221–241, doi:10.1016/S0301-9268(02)00106-7.

Li, Y.-L., 2014, Micro- and nanobands in late Archean and Palaeoproterozoic banded-iron formations as possible mineral records of annual and diurnal depositions. Earth and Planetary Science Letters, v. 391, p. 160–170, doi:10.1016/j.epsl.2014.01.044.

Li, Y.-L., Konhauser, K.O., Kappler, A., and Hao, X.-L., 2013a, Experimental low-grade alteration of biogenic magnetite indicates microbial involvement in generation of banded iron formations. Earth and Planetary Science Letters, v. 361, p. 229–237, doi:10.1016/j.epsl.2012.10.025.

Li, Y.-L., Cole, D.R., Konhauser, K., and Chan, L.S., 2013b, Quartz nanocrystals in the 2.48 Ga Dales Gorge banded iron formation of Hamersley, Western Australia: Evidence for a change from submarine to subaerial volcanism at the end of the Archean. The American Mineralogist, v. 98, p. 582–587, doi:10.2138/am.2013.4205.

Li, Y.-L., Sun, S., and Chan, L.S., 2013c, Phosphogenesis in the 2460 and 2728 million-year-old banded iron formations as evidence for biological cycling of phosphate in the early biosphere. Ecology and Evolution, v. 3, p. 115–125, doi:10.1002/ece3.443.

Liu, H., Wei, Y., and Sun, Y., 2005, The formation of hematite from ferrihydrite using Fe(II) as a catalyst. Journal of Molecular Catalysis, v. 226, p. 135–140, doi:10.1016/j.molcata.2004.09.019.

Meng, D., Wu, X., Fan, F., Meng, X., Zheng, J., and Mason, R., 2009, Submicron-sized fluid inclusions and distribution of hydrous components in jadeite, quartz and symplectite-forming minerals from UHP jadeite–quartzite in the Dabie Mountains, China: TEM and FTIR investigation. Applied Geochemistry, v. 24, p. 517–526, doi:10.1016/j.apgeochem.2008.12.006.

Miyano, T., and Beukes, N.J., 1984, Phase relations of stilpnomelane, ferri-annite and riebeckite in very low-grade metamorphosed iron-formations. Transactions, Geological Society of South Africa, v. 87, p. 111–124.

Morris, R.C., 1980, A textural and mineralogical study of the relationship of iron ore to banded iron-formation in the Hamersley iron province of Western Australia. Economic Geology and the Bulletin of the Society of Economic Geologists, v. 75, p. 184–209, doi:10.2113/gsecongeo.75.2.184.

Morris, R.C., 1993, Genetic modeling for banded iron-formation of the Hamersley Group, Pilbara craton, Western Australia. Precambrian Research, v. 60, p. 243–286, doi:10.1016/0301-9268(93)90051-3.

Morris, R.C., 2012, Microplaty hematite—Its varied nature and genesis. Australian Journal of Earth Sciences, v. 59, p. 411–434, doi:10.1080/08120099.2011.626453.

Morse, J.W., and Casey, W.H., 1988, Ostwald processes and mineral paragenesis in sediments. American Journal of Science, v. 288, p. 537–560, doi:10.2475/ajs.288.6.537.

Mueller, W.U., and Mortensen, J.K., 2002, Age constraints and characteristics of subaqueous volcanic construction, the Archean Hunter Mine Group, Abitibi greenstone belt. Precambrian Research, v. 115, p. 119–152, doi:10.1016/S0301-9268(02)00008-6.

Mueller, W.U., Daigneault, R., Mortensen, J.K., and Chown, E.H., 1996, Archean terrane docking: Upper crust collision tectonics, Abitibi greenstone belt, Quebec, Canada. Tectonophysics, v. 265, p. 127–150, doi:10.1016/S0040-1951(96)00149-7.

Mueller, W.U., Stix, J., Corcoran, P.L., and Daigneault, R., 2009, Subaqueous calderas in the Archean Abitibi greenstone belt: An overview and new ideas. Ore Geology Reviews, v. 35, p. 4–46, doi:10.1016/j.oregeorev.2008.12.003.

Nutman, A.P., and Friend, C.R.L., 2006, Petrography and geochemistry of apatites in banded iron formation, Akilia, W. Greenland: Consequences for oldest life evidence. Precambrian Research, v. 147, p. 100–106, doi: 10.1016/j.precamres.2006.02.005.

Pecoits, E., Gingras, M.K., Barley, M.E., Kappler, A., Posth, N.R., and Konhauser, K.O., 2009, Petrography and geochemistry of the Dales Gorge banded iron formation: Paragenetic sequence, source and implications for palaeo-ocean chemistry. Precambrian Research, v. 172, p. 163–187, doi: 1 0.1016/j.precamres.2009.03.014.

Pickard, A.L., 2003, SHRIMP U-Pb zircon ages for the Palaeoproterozoic Kuruman Iron Formation, Northern Cape Province, South Africa: Evidence for simultaneous BIF deposition on Kaapvaal and Pilbara cratons. Precambrian Research, v. 125, p. 275–315, doi:10.1016/S0301-9268(03)00113-X.

Posth, N.R., Hegler, F., Konhauser, K.O., and Kappler, A., 2008, Alternating Si and Fe deposition caused by temperature fluctuations in Precambrian oceans. Nature Geoscience, v. 1, p. 703–708, doi:10.1038/ngeo306.

Posth, N.R., Koehler, I., Swanner, E.D., Schroeder, C., Wellmann, E., Binder, B., Konhauser, K.O., Neumann, U., Berthold, C., Nowak, M., and Kappler, A., 2013a, Simulating Precambrian banded iron formation diagenesis. Chemical Geology, v. 362, p. 66–73, doi:10.1016/j.chemgeo.2013.05.031.

Posth, N.R., Konhauser, K.O., and Kappler, A., 2013b, Microbiological processes in banded iron formation deposition. Sedimentology, v. 60, p. 1733–1754, doi:10.1111/sed.12051.

Posth, N.R., Canfield, D.E., and Kappler, A., 2014, Biogenic Fe(III) minerals: From formation to diagenesis and preservation in the rock record. Earth-Science Reviews, v. 135, p. 103–121, doi:10.1016/j.earscirev.2014.03.012.

Powell, W.G., Carmichael, D.M., and Hodgson, C.J., 1995, Conditions and timing of metamorphism in the southern Abitibi greenstone belt, Quebec. Canadian Journal of Earth Sciences, v. 32, p. 787–805, doi:10.1139/e95-067.

Rasmussen, B., Fletcher, I.R., Muhling, J.R., Thorne, W.S., and Broadbent, G.C., 2007, Prolonged history of episodic fluid flow in giant hematite ore bodies: Evidence from in situ U-Pb geochronology of hydrothermal xenotime. Earth and Planetary Science Letters, v. 258, p. 249–259, doi:10.1016/j.epsl.2007.03.033.

Rasmussen, B., Meier, D., Krapež, B., and Muhling, J.R., 2013, Iron silicate microgranules as precursor sediments to 2.5-billion-year-old banded iron formations. Geology, v. 41, p. 435–438, doi:10.1130/G33828.1.

Rasmussen, B., Krapež, B., and Meier, D.B., 2014, Replacement origin for hematite in 2.5 Ga banded iron formation: Evidence for postdepositional oxidation of iron-bearing minerals. Geological Society of America Bulletin, v. 126, p. 438–446, doi:10.1130/B30944.1.

Siever, R., 1957, The silica budget in the sedimentary cycle. The American Mineralogist, v. 42, p. 821–841.

Siever, R., 1992, The silica cycle in the Precambrian. Geochimica et Cosmochimica Acta, v. 56, p. 3265–3272, doi:10.1016/0016-7037(92)90303-Z.

Sun, S., Chan, L.S., and Li, Y.L., 2014, Flower-like apatite recording microbial processes through deep geological time and its implication to the search for mineral records of life on Mars. The American Mineralogist, v. 99, p. 2116–2125, doi:10.2138/am-2014-4794.

Taylor, D., Dalstra, H.J., Harding, A.E., Broadbent, G.C., and Barley, M.E., 2001, Genesis of high-grade hematite ore bodies of the Hamersley Province, Western Australia. Economic Geology and the Bulletin of the Society of Economic Geologists, v. 96, p. 837–873, doi:10.2113/gsecongeo.96.4.837.

Viswanathiah, M.N., Tareen, J.A.K., and Krishnamusthy, K.V., 1980, Low temperature hydrothermal synthesis of magnetite. Journal of Crystal Growth, v. 49, p. 189–192, doi:10.1016/0022-0248(80)90081-0.

Walker, J.C.G., 1984, Suboxic diagenesis in banded iron formations. Nature, v. 309, p. 340–342, doi:10.1038/309340a0.

Widdel, F., Schnell, S., Heising, S., Ehrenreich, A., Assmus, B., and Schink, B., 1993, Ferrous iron oxidation by anoxygenic phototrophic bacteria. Nature, v. 362, p. 834–836, doi:10.1038/362834a0.

Wu, W., Swanner, E.D., Hao, L., Zeitvogel, F., Obst, M., Pan, Y., and Kappler, A., 2014, Characterization of the physiology and cell–mineral interactions of the marine anoxygenic phototrophic Fe(II) oxidizer *Rhodovulum iodosum*—Implications for Precambrian Fe(II) oxidation. FEMS Microbiology Ecology, v. 88, p. 503–515, doi:10.1111/1574-6941.12315.

Science Editor: David Schofield
Associate Editor: R.H. Rainbird

Manuscript Received 24 April 2014
Revised Manuscript Received 18 November 2014
Manuscript Accepted 19 December 2014

Printed in the USA

Geological Society of America Bulletin

Primary hematite in Neoarchean to Paleoproterozoic oceans

Si Sun, Kurt O. Konhauser, Andreas Kappler and Yi-Liang Li

Geological Society of America Bulletin 2015;127, no. 5-6;850-861
doi: 10.1130/B31122.1

Notes